

THE BRIGHTEST PULSES IN THE UNIVERSE:  
MULTIFREQUENCY OBSERVATIONS OF THE CRAB PULSAR'S GIANT PULSES

J. M. CORDES

Astronomy Department and NAIC, Cornell University, Ithaca, NY 14853  
cordes@astro.cornell.edu

N. D. R. BHAT

Massachusetts Institute of Technology, Haystack Observatory, Westford, MA 01886  
rbhat@haystack.mit.edu

T. H. HANKINS

Physics Department, New Mexico Institute of Mining & Technology  
thankins@nrao.edu

M. A. MCLAUGHLIN

Jodrell Bank Observatory, University of Manchester, Macclesfield, Cheshire, SK11 9DL, UK  
mclaughl@jb.man.ac.uk

J. KERN

Physics Department, New Mexico Institute of Mining & Technology  
jkern@nrao.edu

*Draft version October 25, 2018*

ABSTRACT

We analyze the Crab pulsar at ten frequencies from 0.43 to 8.8 GHz using data obtained at the Arecibo Observatory and report the spectral dependence of all pulse components and the rate of occurrence of large-amplitude ‘giant’ pulses. Giant pulses occur only in the main-and-interpulse components that are manifest from radio frequencies to gamma-ray energies (known as the ‘P1’ and ‘P2’ components in the high-energy literature). Individual giant pulses reach brightness temperatures of at least  $10^{32}$  K in our data, which do not resolve the narrowest pulses, and are known to reach  $10^{37}$  K in nanosecond-resolution observations (Hankins et al. 2003). The Crab pulsar’s pulses are therefore the brightest known in the observable universe. As such, they represent an important milestone for theories of the pulsar emission mechanism to explain. In addition, their short durations allow them to serve as especially sensitive probes of the Crab Nebula and the interstellar medium. We identify and quantify frequency structure in individual giant pulses using a scintillating, amplitude-modulated, polarized shot-noise model (SAMPNS). The frequency structure associated with multipath propagation decorrelates on a time scale  $\sim 25$  sec at 1.5 GHz. To produce this time scale requires multipath propagation to be strongly influenced by material within the Crab Nebula. We also show that some frequency structure decorrelates rapidly, on time scales less than one spin period, as would be expected from the shot-noise pattern of nanosecond duration pulses emitted by the pulsar. We discuss the detectability of individual giant pulses as a function of frequency and provenance. Taking into account the Crab pulsar’s locality inside a bright supernova remnant, we conclude that the brightest pulse in a typical 1-hour observation would be most easily detectable in our lowest frequency band (0.43 GHz) to a distance  $\sim 1.6$  Mpc at  $5\sigma$ . We also discuss the detection of such pulses using future instruments such as LOFAR and the SKA.

*Subject headings:* Crab pulsar, Crab Nebula, giant pulses, interstellar medium, intergalactic medium

1. INTRODUCTION

Giant pulses from the Crab pulsar are long known (Staelin & Reifenstein 1968) but remain enigmatic tools for probing the pulsar emission mechanism. Recent work has established that giant-pulse fluctuations are most likely associated with changes in the coherence of the radio emission (Lundgren et al. 1995), that giant pulses are broadband (Sallmen et al. 1999), and that they are superpositions of extremely narrow nanosecond-duration structures (Hankins et al. 2003). Giant pulses from the Crab pulsar have the largest implied brightness temperature of any known astrophysical source. A simple estimate for the brightness temperature, based on the

light-travel size and ignoring relativistic dilation, is

$$T_b = \frac{S_\nu}{2k} \left( \frac{D}{\nu \Delta t} \right)^2 = 10^{30.1} \text{ K } S_\nu (\text{Jy}) (\nu_{\text{GHz}} \Delta t_{\mu\text{s}})^{-2} \left( \frac{D}{2 \text{ kpc}} \right)^2, \quad (1)$$

where  $S_\nu$  is the peak flux density at frequency  $\nu$ ,  $D$  is the distance, and  $\Delta t$  is the pulse width. For observed peak amplitudes and pulse widths (e.g.  $10^3$  Jy at 5 GHz with  $\Delta t = 2$  ns; Hankins et al. 2003),  $T_b$  ranges to as high as  $10^{37}$  K.

In this paper we are concerned with the occurrence of giant pulses as a function of frequency and also where they occur as a function of pulse phase. We also establish the properties of the Crab pulsar’s emission in order that

we can estimate the detectability of giant pulse emitters from other galaxies. Detections of such objects would enable studies of pulsar populations in those galaxies and use of the pulses to probe the interstellar medium (ISM) in those galaxies as well as the intervening intergalactic medium. In addition, the Crab pulsar may serve as a prototype of intense, coherent emission from other classes of high-energy objects which may share a similar physical configuration, namely a collimated flow of relativistic particles. As such, the Crab pulsar may signify the presence of other source classes in the transient radio universe that could be targets for proposed widefield telescopes such as LOFAR and the SKA.

In §2 we discuss the observations and issues pertaining to the strong background from the Crab Nebula and to the role of scintillation modulations associated with multipath propagation through the ISM and the Crab Nebula. Average profiles and giant-pulse profiles are discussed in §3 and timing and amplitude statistics in §4. Detectability of giant pulses in other galaxies is summarized in §6 and we conclude the paper in §7. In an Appendix, we discuss frequency structure caused by intrinsic pulse structure and by scintillation.

## 2. OBSERVATIONS

The Crab pulsar was observed at the Arecibo Observatory in January to March and May 2002 using receivers in the Gregorian optical path. Analog signals were analyzed with a fast-dump, real-time correlator system, the Wideband Arecibo Pulsar Processor (WAPP, <http://www.naic.edu/~wapp>), which outputs a data stream of correlation functions at specifiable time intervals. The number of correlation lags (and hence the number of channels across a choice of bandwidths after Fourier transformation) is selectable. The total bandwidth used was 100 MHz for all but 0.43 GHz, where we used 12.5 MHz. We optimized the time resolution by matching the dump time between correlations with the dispersion smearing time across individual channels, subject to a constraint on overall data rate that could be recorded,  $\lesssim 20$  Mbyte  $s^{-1}$ . Table 1 gives the observing parameters: observing frequency,  $\nu$  (GHz); modified Julian date (MJD); total time,  $T$  (hr), of acquired data; total bandwidth,  $B$  (MHz); sample interval,  $\Delta t$  ( $\mu s$ ); channel bandwidth,  $\Delta\nu$  (MHz); dispersion smearing across a single channel,  $\Delta t_{DM} = 8.3 \mu s DM \Delta\nu \nu^{-3}$ ; and the mean system noise,  $S_{sys}$ , expressed in Jy. We used a dispersion measure,  $DM = 56.7910$  pc  $cm^{-3}$ , to dedisperse the data.

Processing consisted of (1) Fourier transforming the correlation functions for each of two polarization channels; (2) summing the resultant spectra for the two polarizations; (3) dedispersing by summing over frequency channels while taking into account time delays associated with plasma dispersion in the ISM; (4) averaging the time series synchronously with the pulsar period to form a standard intensity profile; (5) identifying individual giant pulses and their occurrence times by selecting intensity samples that exceeded the off-pulse mean by  $5\sigma$ ; (6) synchronously averaging the individual giant pulses to form a histogram of giant pulses vs. pulse phase; and (7) aligning average profiles and individual giant pulse profiles in pulse phase by using TEMPO and a spin

model for the Crab pulsar. We also used TEMPO to perform an arrival-time analysis on individual giant pulses, as discussed in §4. For the TEMPO analysis, we used timing models from the Jodrell Bank timing program (<http://www.jb.man.ac.uk/~pulsar/crab.html>).

The procedure for finding giant pulses followed that of Cordes & McLaughlin (2003). The dedispersed time series was first analyzed with the original time resolution and then progressively smoothed and decimated by factors of two in order to approximately match filter to pulses with different widths. In the end, most pulses were optimally detected with no smoothing or only one level of smoothing, as is consistent with the known properties of giant pulses and average profiles (Moffett & Hankins 1996; Sallmen et al. 1999).

### 2.1. Importance of Nebular Background

The Crab Nebula, whose flux density  $\sim 955\nu^{-0.27}$  Jy ( $\nu$  in GHz) (Allen 1973; Bietenholz et al. 1997), dominates the system temperature if it is not resolved by the telescope. Define the system temperature in the absence of the Crab Nebula as  $T_{sys0}$  and the contribution from the Crab Nebula as  $T_{CN}$ . Expressing these in flux density units by dividing by the telescope ‘gain’  $G$  (K  $Jy^{-1}$ ), the total system noise level is

$$S_{sys} = S_{sys0} + S_{CN}. \quad (2)$$

For the Crab pulsar and Nebula, the system temperature is strongly influenced by the Nebula if  $S_{CN} > \epsilon S_{sys0}$  with  $\epsilon = 0.1$ , say. For a single-dish telescope with typical system temperature  $S_{sys0} = 50$  K and 60% aperture efficiency, this condition is satisfied for antenna diameters that satisfy

$$d > 17 \text{ m } \nu^{0.13} \left( \frac{\epsilon T_{sys0}}{50 \text{ K}} \right)^{1/2}. \quad (3)$$

For very large telescopes (either large single-dish antennas or arrays), the effective beam width can be smaller than the Crab Nebula, reducing its contribution to the system noise by a factor  $f_\nu = \Omega_A/\Omega_{CN}$ , where  $\Omega_A$  is the solid angle of the primary antenna beam, and  $\Omega_{CN}$  is the solid angle of the Crab Nebula. The total system noise level is then

$$S_{sys} = S_{sys0} + f_\nu S_{CN}, \quad (4)$$

The characteristic diameter (geometric mean of the major and minor axes) of the Crab Nebula is approximately 5.5 arcmin. For the Arecibo telescope, our data at 0.43 GHz, with beam size equal to 11 arcmin (FWHM) include all of the flux density of the Crab Nebula, while higher frequencies resolve out some of the flux density. The last column of Table 1 indicates our estimate of the system noise including any dilution of the Crab Nebula’s contribution.

In the following, we express pulse amplitudes in terms of the mean system noise.

### 2.2. Scintillations

Diffraction interstellar scintillation (DISS) strongly influences the detectability of the pulsar at frequencies of 3 GHz and higher. There are three regimes that may be identified for scintillation modulations, depending on the size of the scintillation bandwidth,  $\Delta\nu_d$ , relative to

the total bandwidth  $B$  and to the channel bandwidth,  $\Delta\nu$ . For  $\Delta\nu_d \ll \Delta\nu$ , scintillations are essentially quenched because individual ‘scintles’ are averaged out. For  $\Delta\nu \lesssim \Delta\nu_d \lesssim 0.2B$ , scintillations are identifiable as frequency structure in the spectrum of a strong, individual pulse; the net modulation in the dedispersed time series depends on the number of scintles across  $B$  and conforms roughly to a  $\chi^2$  distribution with  $\sim 0.4B/\Delta\nu_d$  degrees of freedom. Finally, for  $\Delta\nu_d \gtrsim 0.2B$ , the dedispersed time series is fully modulated by DISS, with an amplitude modulation factor conforming to a one-sided exponential. The factor,  $0.2B$ , represents the approximate value of  $\Delta\nu_d$  for which we would expect only one scintle within the total bandwidth,  $B$ . Taking into account that  $\Delta\nu_d \propto \nu^{4.4}$ , DISS becomes progressively more important in going to higher frequencies until the scattering becomes weak (in the sense of phase perturbations on the Fresnel scale becoming less than 1 radian; see, e.g., Rickett 1990).

We estimate the DISS bandwidth by using the relation  $2\pi\Delta\nu_d\tau_d = C_1$  (Cordes & Rickett 1998; hereafter CR98), where  $\tau_d$  is the pulse-broadening time and  $C_1$  is a constant dependent on the spectrum and spatial distribution of scattering irregularities; we adopt  $C_1 = 1.05$ , a value appropriate for a thin screen. The pulse-broadening time for the Crab pulsar is known to vary (e.g. Isaacman & Rankin 1975; Lyne & Thorne 1975; Backer et al. 1998; Lyne, Pritchard & Graham-Smith 2001; Backer et al. 2000), ranging from about 0.28 ms to 1.3 ms at 0.3 GHz (Sallmen et al. 1999). Adopting  $\tau_d(0.3 \text{ GHz}) = 0.5$  ms as a reference value, we estimate  $\Delta\nu_d \approx 67 \text{ kHz } \nu^{4.4} [0.5 \text{ ms}/\tau_d(0.3 \text{ GHz})]$ , with  $\nu$  in GHz. Using this expression, we expect that the dedispersed pulse will show fully modulated scintillations (i.e. after summing over the 100 MHz bandwidth) for  $\nu \gtrsim 3.6$  GHz.

We found the mean pulsar flux density (averaged over a few minutes) to be heavily modulated on time scales as short as 5 minutes at frequencies  $\gtrsim 3$  GHz and nearly unchanging at lower frequencies. Such fluctuations are consistent with those expected from DISS, as we discuss in §5. We also saw epoch-to-epoch fluctuations (time scales of one day and longer) that are consistent with refractive interstellar scintillations (RISS), like those identified by Lundgren et al. (1995) at 0.8 GHz on time scales of a few days. The combination of RISS and DISS is particularly strong at 8.8 GHz where the pulsar is undetectable on many days but quite bright, in the mean, on occasional days with DISS fluctuations contributing on shorter time scales. We note that at 8.8 GHz, the diffraction bandwidth  $\Delta\nu_d \approx 1$  GHz (assuming the  $\nu^{4.4}$  scaling), implying that the strength of scattering (as defined in scintillation literature; see Rickett 1990) is not strong and that the DISS and RISS ‘branches’ are not as distinct as at lower frequencies (e.g. Narayan 1992).

### 3. AVERAGE PROFILES

We calculated average profiles of the total intensity by summing partial-sum profiles (of 3 to 12 minutes duration, depending on frequency) in which the largest pulse component had a signal-to-noise ratio (S/N) larger than five and which were unmarred by radio frequency interference (RFI). At frequencies higher than 0.43 GHz, typically only a minority of profiles were included owing to

the effects of DISS or RFI. Likewise, profiles of giant pulse counts were calculated using data subsets corresponding to those included in the average intensity profiles.

Figure 1 shows average intensity and giant-pulse profiles for the ten frequencies journaled in Table 1. The top panel of the pair shown for each frequency is the total intensity profile and the bottom panel shows the giant-pulse histogram vs. pulse phase, i.e. the number of giant pulses in the given pulse phase bin that are above threshold ( $5\sigma$ ). In some of the panels we designate features in the pulse profile, including low-frequency precursor pulse (P), main pulse (MP), interpulse (IP), an intermediate-frequency precursor component (P’; referred to by Moffett & Hankins (1996) as a ‘low-frequency component’); a shifted interpulse component appearing at mid-to-high frequencies (IP’); and two high-frequency components (HFC1 and HFC2) that were first identified by Moffett & Hankins (1996).

We point out the following features of the set of profiles:

1. The pulsar is more readily detectable in its single giant pulses than in the average pulse at all frequencies. This is manifest by the larger S/N in the histogram plots compared to the average profile plots in Figure 1.
2. There is strong evolution of the relative strength of MP and IP as a function of frequency. The ratio of peak IP to peak MP steadily declines from 0.43 to 2 GHz, stays low from 2.5 to 3.5 GHz, and rises at higher frequencies so that the IP is much stronger than the MP at 8.8 GHz.
3. At 4.15 GHz, IP’ appears approximately 0.03 cycles before the location of the lower frequency IP and becomes very strong relative to the MP at 8.8 GHz.
4. At frequencies of 3.5 GHz and higher two new components, HFC1 and HFC2, appear and persist up to the highest frequency we used (8.8 GHz).
5. It is unclear if the HFC1 and HFC2 components are present at 2.15, 2.33 and 2.85 GHz owing to the low S/N of those profiles, which derives from the short integration times and the effects of scintillations.
6. Giant pulses occur only in MP, IP and IP’. For this reason we conclude that IP and IP’ are probably associated with the same physical emitting region or beam in the pulsar.
7. There is more scatter in the pulse phase of the interpulse at high frequencies, manifested in the broader width of the interpulse component. As discussed below in §4, at 8.8 GHz the phase residuals appear to show a two-component distribution, one centered on  $\phi = 0.38$  cycles, the other representing giant pulses skewed toward smaller phases.

Table 2 gives the frequency and total time span used in our analysis in columns 1 and 2; column 3 gives the mean mainpulse-to-interpulse pulse-phase difference; column 4,

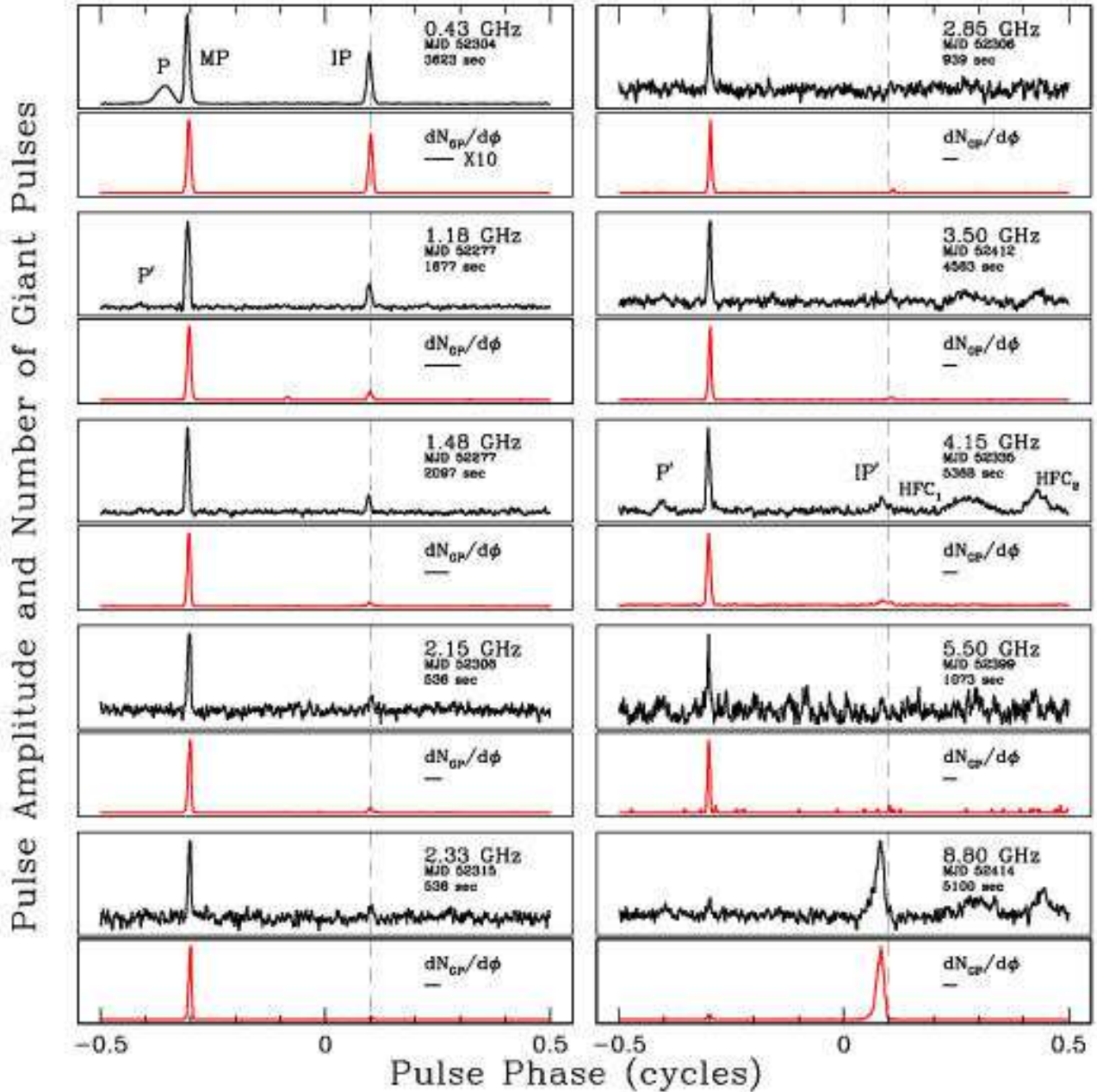


FIG. 1.— Total intensity profiles of the Crab pulsar at 10 radio frequencies. The pair of plots for each frequency is the standard average intensity profile (top) and a histogram of counts of giant pulses plotted against pulse phase (bottom). A threshold of  $5\sigma$  was used to obtain giant pulses included in the histograms. The total integration time is given in the top frame and a horizontal bar designates the net instrumental time resolution, including the effects of dispersion smearing across individual spectrometer channels; the shown bar length is ten times the actual length.



the ratio of the numbers of detected interpulses and mainpulses; and the last column gives the detection rate for events found at  $8\sigma$  or higher. At 0.43 GHz, about 1 in 10 pulses is detected above this level. We emphasize that the detection rate is epoch dependent owing to scintillation modulations. Slow, refractive scintillations affect the rates at all frequencies, while fast diffractive scintillations are particularly important at frequencies above 3 GHz. The 8.8 GHz results apply to a particular day when the scintillation modulation boosted intensities far above their normal level. The mainpulse to interpulse phase difference varies systematically with frequency, remaining constant with frequency (within errors) from 0.43 to 3.5 GHz and then declining with increasing frequency up to 8.8 GHz. This variation in calculated phase difference corresponds to the shift from IP to IP'.

#### 4. AMPLITUDE AND TIMING STATISTICS OF GIANT PULSES

Figures 2 and 3 show histograms of signal-to-noise ratio (S/N) at 0.43 and 8.8 GHz for the main and interpulse components specified in Figure 1. We include only pulses with  $S/N > 8$  in order to provide consistency with the timing analysis discussed below, where we use an  $8\sigma$  threshold for the purpose of obtaining timing residuals minimally influenced by noise. Traditionally, giant-pulse amplitude distributions have been characterized as power laws (e.g. Argyle & Gower 1972; Lundgren et al. 1995). The histograms shown here have roughly power-law segments to their distributions but there are outlier pulses at especially high S/N at both frequencies. Roughly, a power law with slope  $\approx -2.3$  can be drawn through the MP histogram at 0.43 GHz in Figure 2 and a slope  $\approx -2.9$  at 8.8 GHz (Figure 3). These can be compared with slopes of approximately -2.5 at 0.146 GHz (Argyle & Gower 1972) and -3.6 at 0.812 GHz (Lundgren et al. 1995). Overall there thus appears to be steepening of the histogram in going from low to high frequencies. Remarkably, the largest pulse at 0.43 GHz has  $S/N \sim 1.1 \times 10^4$ , which is inconsistent with the probability implied by the power law at lower S/N. We suggest that this pulse is an example of a *supergiant* pulse. The same is true at 8.8 GHz, where giant pulses in the interpulse region are dominant in number but the largest pulse appears in the main pulse component and is  $10\times$  larger than the largest interpulse giant pulse. Conceivably, the largest pulses seen at 0.43 and 8.8 GHz are statistical flukes. The extensive observations of Lundgren et al. (1995) at 0.8 GHz do not indicate the presence of a gap between the brightest and typical giant pulses.

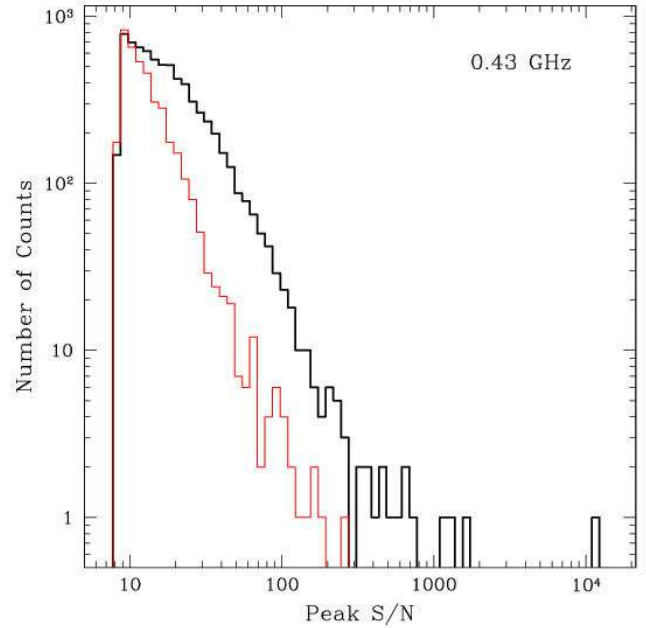


FIG. 2.— Histogram of giant-pulse peak amplitudes at 0.43 GHz. The red curve is for the interpulse and the black curve for the main pulse.

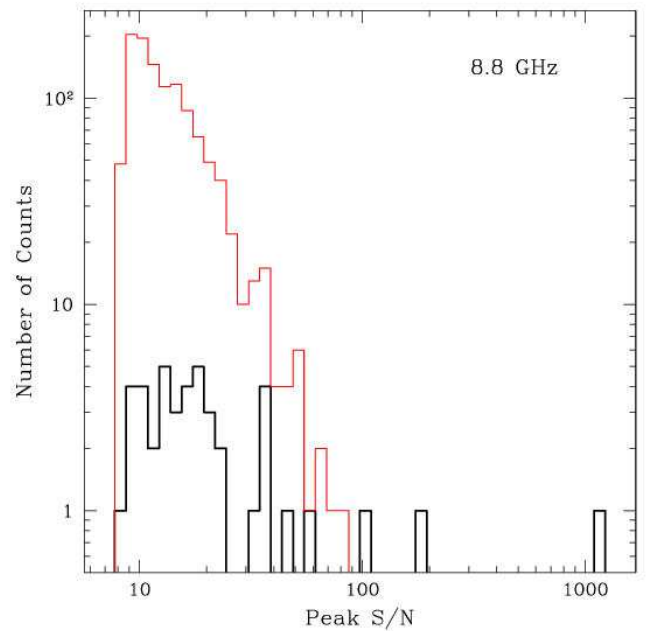


FIG. 3.— Histogram of giant-pulse peak amplitudes at 8.8 GHz. The red curve is for the interpulse and the black curve for the main pulse.

The joint statistics of timing phase residuals and pulse amplitudes (expressed as S/N) are shown in Figures 4 and 5 for the mainpulse and interpulse separately. At the lower frequency (0.43 GHz), the mainpulse phase residuals show a skewed distribution toward larger phases. At 8.8 GHz, the distribution of phase residuals in the interpulse is much broader than in the mainpulse and in either component at 0.43 GHz. This trend is consistent with the appearance of

the average profiles in Figure 1. At 8.8 GHz, the giant interulses showing the most negative phase residuals tend to be weaker than the average. Otherwise, there is no evidence for a strong relationship between amplitude and phase residual.

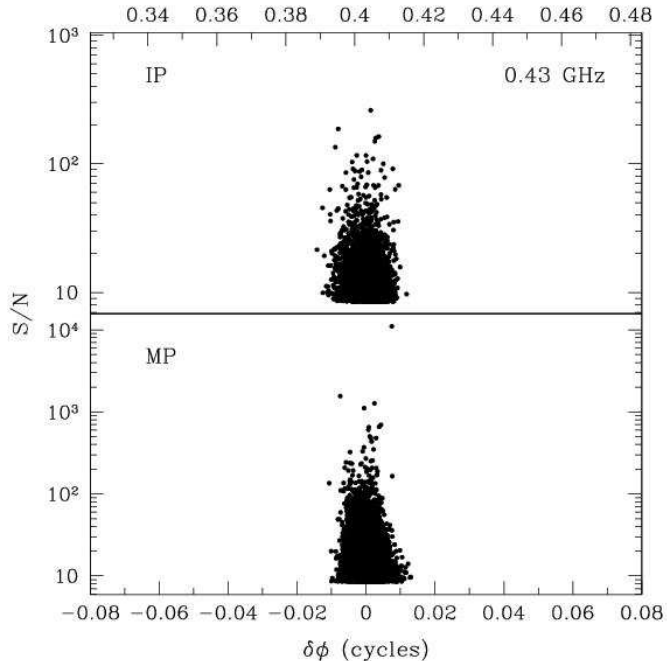


FIG. 4.— Scatter plots of signal-to-noise ratio and pulse phase for 0.43 MHz for the interpulse (IP) and mainpulse (MP). The mean mainpulse phase is defined to be zero.

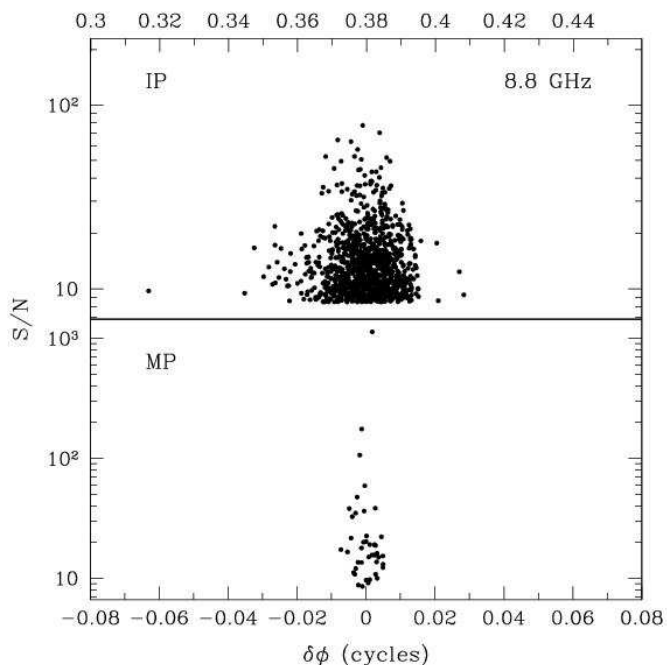


FIG. 5.— Scatter plots of signal to noise ratio and pulse phase residual for 8.8 GHz for the interpulse (IP) and mainpulse (MP).

## 5. SCINTILLATIONS AND SPECTRAL FLUCTUATIONS

From the discussion in §2.2, we estimate that the scintillation bandwidth will range from about 2 kHz at 0.43 GHz to about 1 GHz at 8.8 GHz if we assume a scaling  $\Delta\nu_d \propto \nu^{4.4}$ . Previous work also suggests that at any epoch the actual scintillation bandwidth could vary by a factor of a few about these values. Such variations are due to the stochastic nature of the process but also are caused by refractive modification of the diffraction parameters (e.g. Rickett 1990). At our lowest frequency, 0.43 GHz, the DISS bandwidth is about 1/10 the channel bandwidth (c.f. Table 1). Thus, the brightest features in the frequency-time data are expected to be diminished by the smoothing implied by the spectrometer resolution. At our highest frequency, 8.8 GHz, the predicted DISS bandwidth is a factor of eight smaller than the center frequency, signifying that scintillations are in the transition regime between strong and weak scattering. In the transition regime, we expect deep modulations as in the strong scattering regime, but with different statistics and, according to our estimate, they will be highly correlated across our 100 MHz bandwidth.

Of course, our predictions for DISS bandwidth require some caveats. First, our data were obtained over a 0.4 year period over which time the scattering strength undoubtedly varied, probably yielding an implied pulse-broadening time at 0.43 GHz different from the value we have assumed (100  $\mu$ s). Second, the scaling with frequency of the DISS quantities may depart from that which has been identified along other lines of sight in the ISM. The scaling with the 4.4 exponent has been established for pulsars with small DMs, while a few objects show a weaker scaling as  $\nu^4$ . Recent work on high-DM pulsars (Löhmer et al. 2001; Bhat et al. 2003) indicates that the pulse broadening time may vary as weakly as  $\nu^{-3}$  (and the scintillation bandwidth thus as  $\nu^3$ ). However, it is also clear from Bhat et al. (2003) that empirical determinations of the exponent are sensitive to assumptions about the form of the pulse-broadening function fitted to the data and how it interacts with the assumed intrinsic pulse shape of the pulsar. Nonetheless, despite these uncertainties, evidence suggests that the pulse broadening from the Crab pulsar is not only highly variable, but often exceeds the predictions based on lower frequencies using either of the strong scaling laws,  $\Delta\nu_d \propto \nu^4$  or  $\nu^{4.4}$ . Possible interpretations include contributions from scattering within the pulsar magnetosphere (Hankins & Moffett 1998) or from scattering regions within the Crab Nebula that are bounded spatially (Cordes & Lazio 2001). Spatially bounded scattering regions can generate scattering times that scale with frequency differently than with an exponent of 4 or 4.4.

In Figures 6 - 10 we show plots of the pulsed flux for single giant pulses in the frequency-time plane, the pulse shape obtained by summing over frequency both with and without compensation for dispersion delays, and the spectrum of the pulse.

At 0.43 GHz, the pulse is easily detected even without dedispersion owing to the high S/N. Structure in the spectrum is quite spiky and is associated with individual scintles caused by DISS. This is so, in spite of the fact that the DISS bandwidth is substantially smaller than the channel bandwidth, because the spacing between scintles

is quite large. DISS in the strong scattering regime is exponentially distributed and with an ensemble average mean modulation of unity. Consistent with the statistics is the estimate that the number of strong scintles within a bandwidth  $B$  is

$$N_\nu \approx 1 + 0.2B/\Delta\nu_d. \quad (5)$$

As can be seen in the right-hand panel of Fig 6, the minimum spectral values away from the bandpass edges are well offset from zero, signifying that the overall modulation is less than the 100% expected from exponential DISS statistics, consistent with the smoothing of scintles that occurs in the process of channelizing the data.

By comparison, plots of giant pulses at 1.5 and 2.4 GHz (Figures 7 and 8) show minimum spectral values nearly equal to zero flux density, consistent with the larger, nearly-resolved or resolved scintillation structure expected at those frequencies. At 2.85 GHz, the minimum spectral values are well above zero, signifying that the DISS bandwidth is large enough that only one or two scintles are expected across the band. At 8.8 GHz (Figure 10), the modulation of the flux across the bandpass has a much different character, as expected if  $\Delta\nu_d \gg B$ , where  $B = 100$  MHz.

### 5.1. Scintillation Bandwidths

We estimate the scintillation bandwidth by calculating the intensity autocorrelation function,  $A(\delta\nu) = \langle I(t, \nu)I(t, \nu + \delta\nu) \rangle$  for the spectrum of each giant pulse and summing over giant pulses. For this analysis, we used giant pulses with signal to noise ratios  $S/N > 20$  in the dedispersed pulse. Scintillation structure is unresolved at frequencies below 2 GHz and is comparable to or larger than our receiver bandpass at frequencies larger than 4 GHz. Results are shown in Table 3 along with scintillation time scales, discussed in the next section, and the number of giant pulses used to estimate the parameters.

FIG. 6.— Plot of intensity against time and frequency, showing a single dispersed pulse as it arrives at different frequencies centered on 0.43 GHz. The right-hand panel shows the pulse amplitude vs. frequency while the bottom panel shows the pulse shape with and without compensating for dispersion delays. This pulse is the largest in one hour of data, has  $S/N \sim 1.1 \times 10^4$ , and a pulse peak that is 130 times the flux density of the Crab Nebula, or  $\sim 155$  kJy. Note that the segments at either end of the bandpass where the pulse arrival time is opposite the trend at most frequencies is caused by aliasing of the signal.

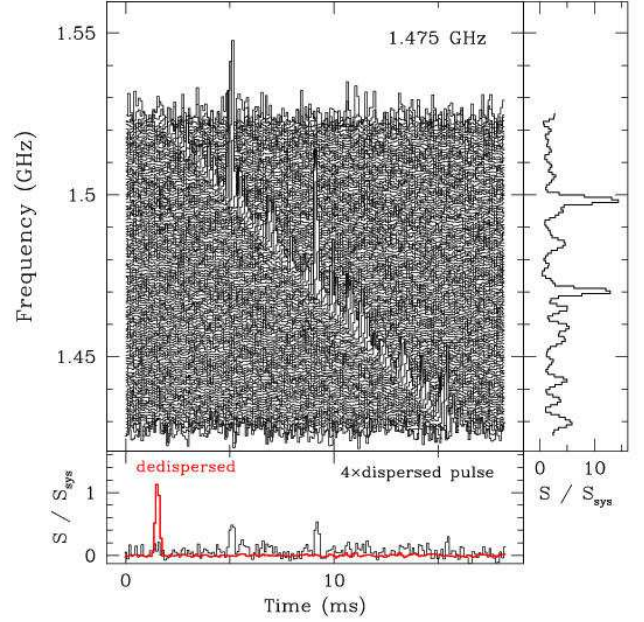


FIG. 7.— Same as Fig. 6 for a single pulse at 1.475 GHz. This pulse is the largest in one hour of data, has  $S/N \sim 225$ , and a pulse peak that is 1.2 times the mean system noise, or  $\sim 1.03$  kJy. Note that individual ‘scintles’ in the spectrum reach 14 times  $S_{\text{sys}}$ , or 4.1 kJy.

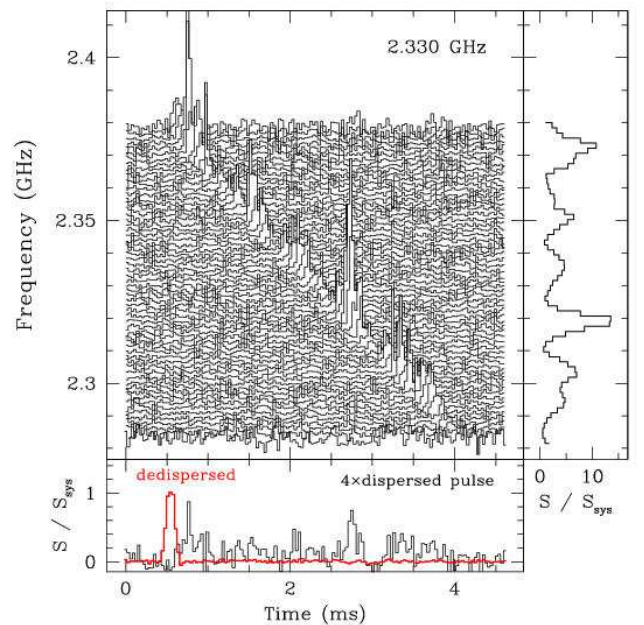
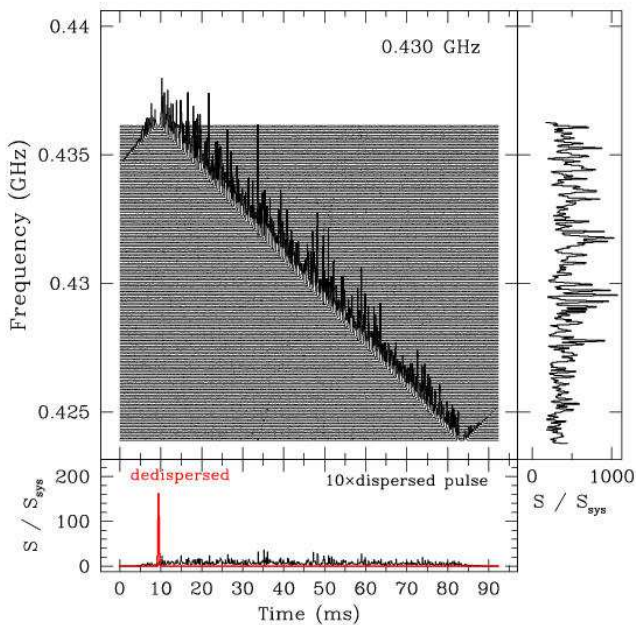




FIG. 8.— Same as Fig. 6 for a single pulse at 2.33 GHz. This pulse is the largest in one hour of data, has  $S/N \sim 161$ , a pulse peak that is  $1.1S_{\text{sys}}$ , and a scintillation peak  $\sim 12S_{\text{sys}}$ . At this frequency the telescope beam resolves the Crab Nebula, so the peak flux densities are  $\sim 86$  and  $\sim 936$  Jy in the dedispersed pulse and spectrum, respectively.

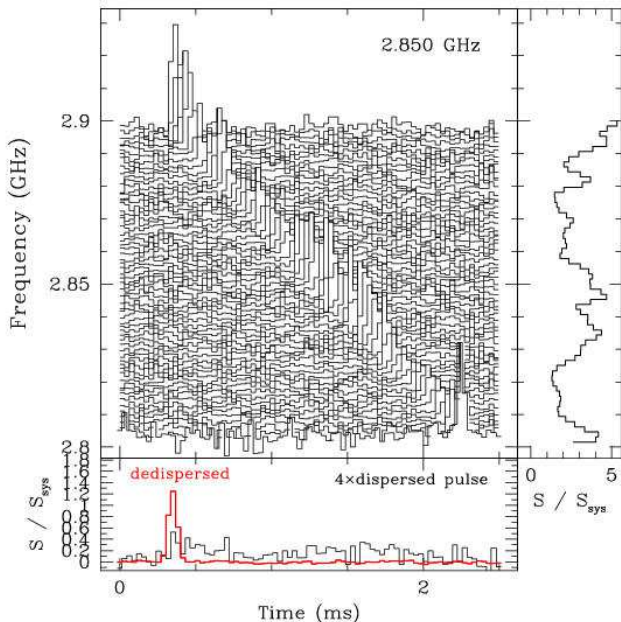


FIG. 9.— Same as Fig. 6 for a single pulse at 2.85 GHz. This pulse is the largest in one hour of data, has  $S/N \sim 111$ , a pulse peak that is  $1.2S_{\text{sys}}$ , and a scintillation peak  $\sim 4.5S_{\text{sys}}$ . At this frequency the telescope beam resolves the Crab Nebula, so the peak flux densities are  $\sim 89$  and  $\sim 333$  Jy in the dedispersed pulse and spectrum, respectively.

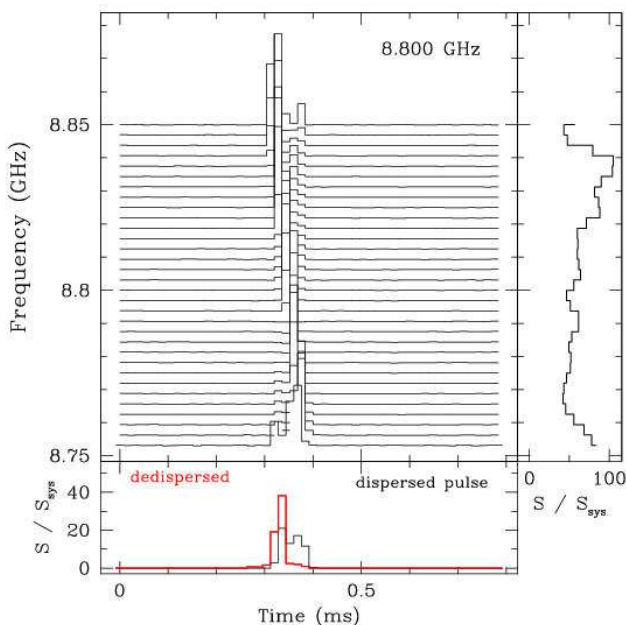


FIG. 10.— Plot of intensity against time and frequency, showing a single dispersed pulse as it arrives at different frequencies centered on 8.8 GHz. The right-hand panel shows the pulse amplitude vs. frequency while the bottom panel shows the pulse shape with and without compensating for dispersion delays. This pulse is the largest in one hour of data, has  $S/N \sim 1.3 \times 10^3$ , a pulse peak that is  $\sim 40S_{\text{sys}}$ , and a spectral peak  $\sim 100S_{\text{sys}}$ . At this frequency the telescope beam resolves the Crab Nebula. The peak flux densities are  $\sim 880$  and  $\sim 2.2 \times 10^3$  Jy in the dedispersed pulse and spectrum, respectively.

## 5.2. Scintillation Time Scale

The scintillation time scale is the time for features in the diffraction pattern to transport across the line of sight (LOS), combined with any reorganization of the diffraction pattern itself. These two contributions are determined by the velocities of the source and observer and any bulk motion of the intervening material, which change the sampling geometry of the diffraction pattern, combined with random velocities in the medium. Traditionally the scintillation time scale is calculated as the  $e^{-1}$  width along the time lag axis of the two dimensional intensity correlation function,  $C(\delta\nu, \tau) = \langle I(t, \nu)I(t + \tau, \nu + \delta\nu) \rangle$ . For strong pulsars with steady pulse emission and scintillation time scales of minutes or longer,  $C(\delta\nu, \tau)$  can be calculated on a uniform grid of  $\delta\nu$  and  $\tau$ . However, for the Crab pulsar, the giant pulses allow only sporadic sampling along the time-lag axis. At most of our observing frequencies, it is difficult to establish values for  $\Delta t_d$  either because the DISS frequency structure is unresolved (e.g. at 0.43 GHz) or because we cannot find enough close pairs of giant pulses having adequate  $S/N$  to estimate reliably the correlation coefficient of the spectra. However, at 1.475 GHz and 2.33 GHz, detectable pulses allow us to estimate  $\Delta t_d$ .

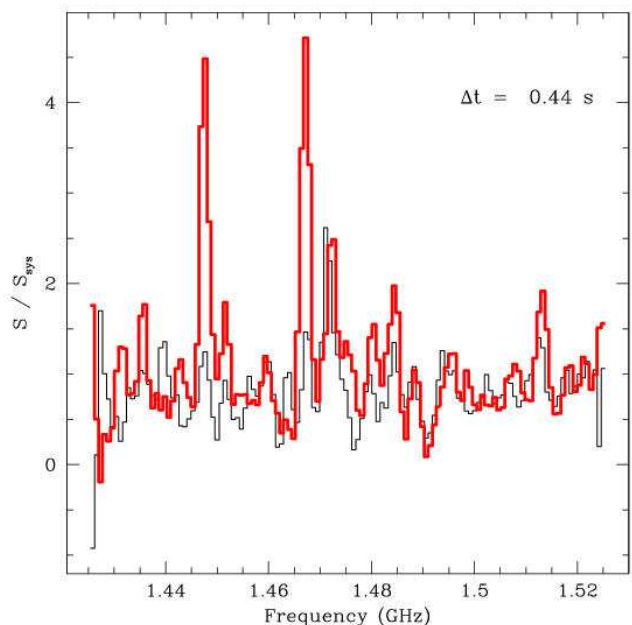




FIG. 11.— Plot showing spectra for two giant pulses spaced by  $\Delta t = 0.44$  sec and having S/N of 66 and 82 (defined as peak to rms in the dedispersed time series) for the curves with the light and heavy lines, respectively. The largest spectral peaks in the stronger pulse have S/N  $\approx 100$ . Additive radiometer noise therefore contributes very little to the spectral structure shown here. Features in the spectra for the two pulses align in frequency but have very different amplitudes. The correlation coefficient between the two spectra is 0.46. As discussed in the Appendix, some of the frequency structure is caused by DISS while other structure is associated with the intrinsic noise properties of the pulse.

Figure 11 shows spectra for a close pair of high S/N pulses at 1.475 GHz. While some of the features in the spectra align, it is clear that the frequency structure has decorrelated significantly. The correlation coefficient is only 0.46. If scintillations were the only source of frequency structure, this would imply an exceedingly short decorrelation time. However some of the frequency structure is associated with the intrinsic noise of the pulsar signal. (Little structure is associated with additive radiometer noise owing to the high S/N of 66 and 82 for the dedispersed pulses.) The intrinsic frequency structure has a frequency scale  $\Delta\nu_i \approx W_A^{-1}$ , where  $W_A$  is the characteristic pulse width. With  $W_A \approx 100 \mu\text{s}$ , the intrinsic structure is expected to show  $\Delta\nu_i \approx 10$  kHz, much narrower than the channel bandwidth of 0.78 MHz. However, substructure within the pulse envelope comprising short-duration pulses of duration  $1 \mu\text{s}$  or less would increase this scale to 1 MHz or more. Hankins et al. (2003) have identified substructure in giant pulses on these short time scales. We conclude that the intrinsic pulse structure is responsible primarily for the fast decorrelation between the pair of pulses. This conclusion is corroborated by a statistical study of a large number of pulse pairs.

Figure 12 shows the correlation coefficient  $C(0, \tau)$  between a large number of pulse pairs plotted against time separation,  $\tau$ . We have used only those pulses with S/N  $> 20$  in the dedispersed pulse in order to reduce scatter in the correlation estimates from additive noise. The roll-off of the correlation coefficient at larger lags represents a correlation time,  $\Delta t_d \approx 25 \pm 5$  sec at 1.475 MHz. From Appendix A, we expect the asymptotic correlation coefficient (at small lags) to be  $1/(2 + d_p^2)$ , in the mean, under the scintillating amplitude-modulated shot-noise (SAMPSN) model and where  $d_p$  is the degree of polarization ( $\leq 1$ ). This level is consistent with the level of correlation seen at lags  $\tau \lesssim 1$  sec if the pulses are typically highly polarized. Consistency of giant pulse spectral statistics with SAMPSN implies that, typically, pulses at 1.475 GHz are composed of a large number ( $\gtrsim 5$ ) of individual shot pulses in order that the intrinsic fluctuations are Gaussian and thus contribute to the rapid decorrelation seen (see Appendix).

A similar analysis for 2.33 GHz data yields a somewhat longer time scale (Table 3). At still higher frequencies, there are insufficient pairs of strong pulses to establish the correlation time, though we are able to estimate the scintillation bandwidth up to 3.5 GHz. At 8.8 GHz, where the scintillation bandwidth is larger than the observation bandwidth, we expect spectral modulations to derive solely from amplitude-modulated noise statistics (combined with radiometer noise), implying that the modulation index  $m_I = \sigma_I/I = \sqrt{(1 + d_p^2)/2}$  (after

correction for any contribution from radiometer noise, which is negligible for the largest pulses). For the pulse displayed in Figure 10, the modulation index is only 0.29. A low modulation index suggests that the giant pulse of that figure is dominated by a single shot pulse with duration comparable to the reciprocal bandwidth,  $\sim 10$  ns, or that the giant pulse comprises a cluster of shot pulses with a similar width. Such results are not inconsistent with those of Hankins et al. (2003), who found nanosecond structure within individual giant pulses at 5 GHz.

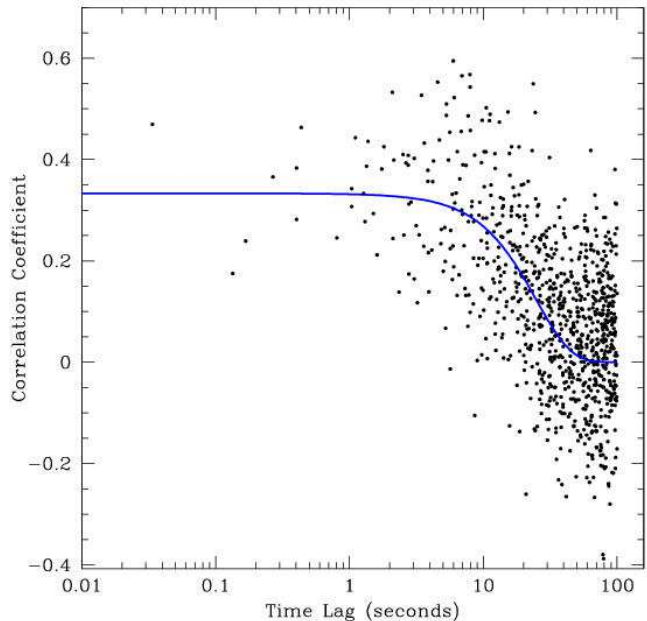


FIG. 12.— Plot of the correlation coefficient  $C(\delta\nu = 0, \tau)$  vs. time lag  $\tau$  between spectra of giant pulses at 1.475 GHz, where  $\tau$  is the time separation between pairs of giant pulses. At this frequency, the number of close pairs is sufficient to establish that frequency structure in the spectra is correlated over short time scales, with an  $e^{-1}$  time scale  $\approx 25 \pm 5$  s. The smallest lag occurs at one of the quantized values determined by the spacing of the mainpulse and interpulse components. The line represents the mean correlation function expected for scintillating amplitude modulated shot noise with a correlation time of 25 sec.

### 5.3. Scintillation Speed

The effective speed with which the intensity pattern caused by multipath propagation crosses the LOS can be estimated from the scintillation bandwidth and time scale. If we assume that electron density fluctuations have a Kolmogorov spectrum and fill the LOS uniformly, the pattern speed is (CR98)

$$V_{\text{ISS},5/3,u} = A_{\text{ISS},5/3,u} \frac{\sqrt{D\Delta\nu_d}}{\nu\Delta t_d}, \quad (6)$$

with  $A_{\text{ISS},5/3,u} = 2.53 \times 10^4 \text{ km s}^{-1}$  for  $\nu$  in GHz,  $\Delta t_d$  in s,  $\Delta\nu_d$  in MHz and  $D$  in kpc. We evaluate  $V_{\text{ISS},5/3,u}$  at 1.475 GHz by using the decorrelation time estimated in the previous section but by scaling the scintillation bandwidth from 2.33 GHz, since it is unresolved at 1.475 GHz. Scaling from 2.33 GHz using  $\Delta\nu_d \propto \nu^{4.4}$ , we obtain  $\Delta\nu_d \approx 0.31 \pm 0.05$  MHz. Using  $D = 2$  kpc for the distance to the Crab Nebula, the scintillation speed is  $V_{\text{ISS},5/3,u} \approx 540 \text{ km s}^{-1}$ . Under the assumptions leading to

this estimate,  $V_{\text{ISS},5/3,u}$  should be approximately equal to the transverse pulsar speed,  $|\mathbf{V}_{\text{p}\perp}| \approx 171 \pm 28 \text{ km s}^{-1}$  from an HST proper motion measurement (Caraveo & Mignani 1999); instead, there is a factor of 3 discrepancy.

No element in the scattering geometry (pulsar, medium, or source) has a velocity as large as  $V_{\text{ISS},5/3,u}$  and it is reasonable to conclude that the scattering medium is in fact not uniform along the LOS, receiving contributions from the Crab Nebula’s filaments. First, we ignore the effects of the general ISM and consider filamentary scattering screens at a distance  $D_s \approx 1 \text{ pc}$  from the pulsar. Then, using Equations 13-18 of CR98 to correct for the geometric leveraging effects of screen(s) near the pulsar, we obtain

$$V_{\text{ISS}} = W_C \left[ \frac{2(D - D_s)}{D_s} \right]^{1/2} V_{\text{ISS},5/3,u} \quad (7)$$

$$\approx 3.4 \times 10^4 \left( \frac{D/D_s}{2000} \right) \text{ km s}^{-1},$$

where we have used  $W_C \approx 1.05$  (c.f. Figure 1 of CR98).

For a thin screen, the pattern speed is related physically to the velocities of the pulsar, observer, and medium as (CR98, equation 4)  $V_{\text{ISS}} = (D/D_s)|\mathbf{V}_{\text{eff},\perp}|$ , or,

$$V_{\text{ISS}} = \left| \left( \frac{D}{D_s} - 1 \right) \mathbf{V}_{\text{p}\perp} + \mathbf{V}_{\text{obs}\perp} - \left( \frac{D}{D_s} \right) \mathbf{V}_{\text{m}\perp} \right|, \quad (8)$$

where  $\mathbf{V}_{\text{p}\perp}$ ,  $\mathbf{V}_{\text{obs}\perp}$ ,  $\mathbf{V}_{\text{m}\perp}$  are the transverse velocities of the pulsar, observer and medium relative to the local standard of rest. The pulsar and medium’s velocities are “boosted” by the factor  $D/D_s \approx 2000$ , so we may ignore the Earth’s motion in the following.

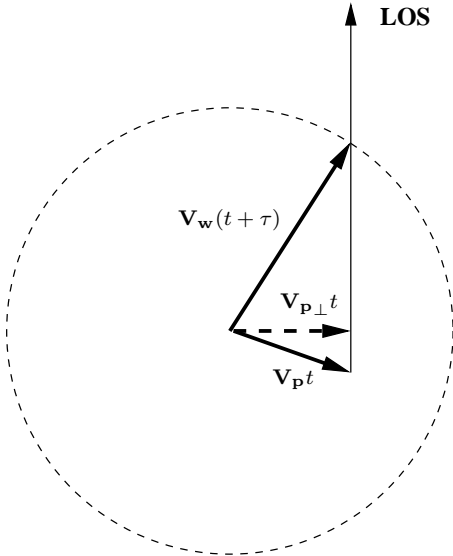


FIG. 13.— Geometry showing the line of sight to the present-day location of the pulsar, which has moved a distance  $\mathbf{V}_{\text{p}} t$  over the time  $t$  since the supernova explosion, while the present day location of stellar wind material along the line of sight is at a location  $\mathbf{V}_{\text{w}}(t+\tau)$ , taking into account an additional time  $\tau$  prior to the supernova explosion during which the progenitor wind was active. Under the assumption of radial motion of the wind, the wind material (or blast-wave material condensed into filaments) has a transverse speed  $\mathbf{V}_{\text{w}\perp} = \mathbf{V}_{\text{p}\perp}/(1 + \tau/t)$ .

The LOS filament velocities are  $\lesssim 1500 \text{ km s}^{-1}$  (Fesen & Kirshner 1982). To estimate the effective transverse

velocity, we need to consider the symmetry of filament motions and how the geometry has changed since the supernova explosion. Figure 13 shows the geometry under the assumption of purely radial motion by wind material (which may represent a pre-supernova wind or blast-wave material). The present-day transverse velocity of the pulsar implies transverse filament velocities  $\mathbf{V}_{\text{fil}\perp} \equiv \mathbf{V}_{\text{p}\perp}$  (for filament segments along the present-day LOS to the pulsar) if filaments originally had strictly radial velocities (relative to the explosion center). In this case,  $\Delta\mathbf{V}_{\text{pf}\perp} \equiv \mathbf{V}_{\text{p}\perp} - \mathbf{V}_{\text{fil}\perp}$  vanishes and the effective transverse speed is merely the pulsar speed.

However, nonradial filament motions are expected because the pulsar’s progenitor star was rotating. Even with fairly slow rotation, nonradial filament speeds of a few  $\text{km s}^{-1}$  are boosted by the factor  $D_s/D$  to several thousand  $\text{km s}^{-1}$ . Faster rotation yields accordingly faster transverse filament speeds today. Filaments may also have arisen from material in or deflected by a circumstellar disk around the progenitor (Fesen, Martin, & Shull 1992), again yielding large nonradial filament speeds today. Alternatively, the material responsible for scattering in the Crab Nebula could derive from the presupernova wind. In any case, we assume that  $\Delta V_{\text{pf}\perp}$  is nonnegligible. It is not clear if nonradial filamentary motions have been detected directly or not in the Crab Nebula (MacAlpine et al. 1994; Schaller & Fesen 2002). However, indirect constraints (Trimble 1968; see also discussion in Backer, Wong & Valanju 2000) based on filament motions with respect to the explosion center allow nonradial motions  $\sim 70 \text{ km s}^{-1}$ .

By equating Eq. 7 and 8, we derive a constraint (independent of the distance to the Crab Nebula),

$$\Delta V_{\text{pf}\perp} = \sqrt{2} W_C V_{\text{ISS},5/3,u} \left( \frac{D_s}{D} \right)^{1/2} \quad (9)$$

$$\approx 18 D_s^{1/2} \text{ km s}^{-1}.$$

For pulsar-filament distances  $D_s = 1 \text{ pc}$ , transverse filament speeds relative to the pulsar  $\approx 18 \text{ km s}^{-1}$  are needed. We conclude that filaments that affect the pulsar’s radio emission possess modest nonradial motions relative to the explosion center.

Alternatively, we can consider the combined effects of filaments in the Crab Nebula and the general ISM. Calculating the weighting factor  $W_{\text{D,ISS}}$  that relates  $V_{\text{ISS}}$  to  $V_{\text{ISS},5/3,u}$  (c.f. Eq. 10-18 of CR98) while taking into account a uniform ISM combined with a thin screen, we find an expression analogous to that in Eq. 9,

$$\Delta V_{\text{pf}\perp} \approx (3/8)^{3/5} W_C V_{\text{ISS},5/3,u} \left( \frac{\text{SM}_{\text{ISM}}}{\text{SM}_{\text{CN}}} \right)^{3/5}, \quad (10)$$

where  $\text{SM}_{\text{ISM}}$  and  $\text{SM}_{\text{CN}}$  are the scattering measures for the general ISM and the Crab Nebula, respectively, and we have assumed that  $(D_s/D) \text{SM}_{\text{ISM}} \gg \text{SM}_{\text{CN}}$  but that  $\text{SM}_{\text{CN}} > \text{SM}_{\text{ISM}}$ . The scattering measure is the LOS integral of  $C_n^2$ , the spectral coefficient for electron density irregularities (e.g. Cordes & Lazio 2002). Using values inferred for the two scattering measures (from, e.g., the electron density model, NE2001, of Cordes & Lazio 2002 and from pulse broadening of the Crab Nebula), Eq. 10 yields an estimate  $\Delta V_{\text{pf}\perp} \approx 20 \text{ km s}^{-1}$  similar to that using Eq. 9.

## 6. DETECTABILITY OF GIANT PULSES FROM EXTRAGALACTIC CRAB-LIKE PULSARS

The pulses we have identified are sufficiently strong to be detected from other galaxies. If we were to place the Crab pulsar in another galaxy, the inverse square law would lessen pulse amplitudes but so too would it decrease the contribution to the system temperature from the Crab Nebula. Consider a Crab-like pulsar in a Crab-Nebula-like nebula at distance  $D_{\text{Neb}}$ . The system noise level for this object is (assuming it to be unresolved)

$$S_{\text{sys}} = S_{\text{sys}_0} + \left(\frac{D_{\text{CN}}}{D_{\text{Neb}}}\right)^2 S_{\text{CN}}. \quad (11)$$

The nebular contribution to the system noise becomes less than the nominal system noise if  $S_{\text{sys}} < (1 + \epsilon)S_{\text{sys}_0}$  or

$$D_{\text{Neb}} > D_{\text{CN}} \left(\frac{S_{\text{CN}}}{\epsilon S_{\text{sys}_0}}\right)^{1/2}. \quad (12)$$

Table 4 shows values of  $D_{\text{Neb}}$  that satisfy inequality 12 for the Arecibo Telescope, the Green Bank Telescope (GBT), the VLA (and the Extended VLA), the Allen Telescope Array, the Low-Frequency Array (LOFAR), and the Square Kilometer Array (SKA). In all cases, we assume the nebula is unresolved. For the VLA, the ATA, LOFAR and some designs for the SKA, this assumption will break down. For  $\epsilon = 1$  (equal contributions to  $S_{\text{sys}}$  from the nebula and from receiver and background noise), the Nebula is unimportant for objects in the Magellanic Clouds for either of the existing telescopes. However, for the SKA, nebular noise is dominant for such objects. For the largest nearby spiral galaxies (M31 and M33), however, nebular noise is negligible for all existing and contemplated telescopes.

The optimal frequency can also be determined. If we assume that the spectrum is the same as that of the Crab pulsar, lower frequencies are favored unless propagation effects smear the pulse. For the Crab pulsar itself, 0.43 GHz is approximately the lowest frequency at which propagation effects are sufficiently small. For pulsars in M31 or M33, the dispersion measures expected given their respective Galactic latitudes and inclinations are approximately equal to the DM of the Crab pulsar. Similarly, the scattering is expected to be approximately the same. Consequently, we can use our 0.43-GHz results on the Crab pulsar to estimate the  $S/N$  expected for extragalactic emitters of giant pulses.

The strongest pulse observed at 0.43 GHz has  $S/N_{\text{max}} = 1.1 \times 10^4$  even with the system noise dominated by the Crab Nebula. For objects in M31 ( $D \approx 0.8$  Mpc) or further, the system noise is essentially unaffected by the nebular contribution. If the Crab pulsar were not embedded in its nebula, the  $S/N$  of our largest pulse would have been  $S_{\text{CN}}/S_{\text{sys}_0} \approx 300$  times larger, or  $3.3 \times 10^6$ . For this particular pulse, the maximum distance it could be detected at a specified signal-to-noise ratio,  $(S/N)_{\text{det}}$  is

$$D_{\text{max}} = D_{\text{CN}} \left[ \frac{(S/N)_{\text{max}}}{(S/N)_{\text{det}}} \left(1 + \frac{S_{\text{CN}}}{S_{\text{sys}_0}}\right) - \frac{S_{\text{CN}}}{S_{\text{sys}_0}} \right]^{1/2} \quad (13)$$

$$\approx 1.6 \text{ Mpc} \left[ \frac{(S/N)_{\text{det}}}{5} \right]^{-1/2}. \quad (14)$$

The largest 0.43 GHz pulse would thus be detectable from M33 ( $D \approx 0.93$  Mpc) using the Arecibo telescope

and our current spectrometer at  $S/N \approx 15$ . Using the GBT to observe M31 (since M31 is outside the declination range of Arecibo), our largest pulse would have  $S/N \approx 4.8$ . Thus, a convincing detection of giant pulses from M31 with the GBT would require longer dwell times than one hour in order that yet-stronger pulses could be detected. Detection of giant pulses is discussed in general in Cordes & McLaughlin (2003) and in particular from nearby galaxies in McLaughlin & Cordes (2003).

LOFAR (the Low-frequency Array) would allow detection of a giant pulse at 0.2 GHz at the  $5\sigma$  level out to a distance of 1.5 Mpc for our largest pulse at 0.43 GHz, scaled to 0.2 GHz. The SKA would yield  $D_{\text{max}} \approx 5.9$  Mpc for a  $5\sigma$  detection of our largest pulse at 0.43 GHz. There are approximately 16 galaxies (of M33's size or larger) within this distance. If pulsars like the Crab pulsar persist in emitting giant pulses for a time of order the current age of the Crab ( $\sim 10^3$  yr) and if the birth rate of pulsars scales as the ratio of a galaxy's mass to the Milky Way's mass,  $\dot{N}_{\text{psr}} \approx 10^{-2} \text{ yr}^{-1} M_{\text{gal}}/M_{\text{MW}}$ , we expect that there should be a few to about 20 such pulsars in each of these galaxies. Of course, giant-pulses are also emitted by millisecond pulsars whose magnetic fields at their light cylinders are comparable to that of the Crab pulsar (Cognard et al. 1996; Johnston & Romani 2002) so the numbers of detectable objects may be larger. At present, however, the Crab pulsar emits the most luminous giant pulses of any of these objects and best serves as a prototype for detectable objects from other galaxies.

## 7. SUMMARY & CONCLUSIONS

We have shown that giant pulses from the Crab pulsar are restricted to only two of the pulse components seen in long-term average profiles. These components are the same as those detected at optical, X-ray and gamma-ray energies, suggesting that the mechanism for giant-pulse emission occurs high in the magnetosphere, where these emissions are expected to originate. The occurrence of giant pulses is strongly frequency dependent. We find that giant pulses 'follow' the interpulse in pulse phase as it shifts to earlier phases above  $\sim 4$  GHz. We therefore conclude that the same physical region produces both the low-frequency and the shifted, high-frequency interpulse. While the main pulse is dominant from 0.43 to 5.5 GHz, both in the average profiles and in the number of giant pulses, at 8.8 GHz, the interpulse is dominant. We have no clear interpretation of this trend other than the usual suspect processes: beaming and spectral dependence. It is our aim to analyze the profile shapes and giant-pulse occurrence histograms along with multiwavelength pulse profiles extending to  $> 100$  MeV gamma-rays in order to better constrain the roles of beaming and coherence mechanisms. This work will be deferred to another paper.

Epoch dependence of the giant-pulse rate derives from scintillation effects that appear to be strongly influenced by plasma in the Crab Nebula. Backer, Wong & Valanju (2000) demonstrate that multiple images occur owing to the passage across the line of sight of refracting plasma. We establish the scintillation time scale that is sufficiently short ( $\sim 25$  s at 1.48 GHz) that plasma relatively near the pulsar (i.e. inside the Crab Nebula) is required.



Our analysis on giant-pulse amplitudes suggests that, to the extent that the Crab pulsar serves as a prototype of giant-pulse emission, giant pulses from extragalactic pulsars should be detectable out to large distances  $\sim 1.6$  Mpc at Arecibo with existing back-end spectrometers.

We thank Bill Sisk and Jeff Hagen for developing the WAPP system at the Arecibo Observatory, which was crucial for providing the data analyzed in this paper. We thank Mal Ruderman for helpful discussions. NDRB

is supported by an MIT-CfA Postdoctoral Fellowship at Haystack Observatory. Work at Cornell University was supported by NSF grants AST 9819931 and 0206036. MAM was also supported by an NSF MPS-DRF Fellowship. This work was also supported by the National Astronomy and Ionosphere Center, which operates the Arecibo Observatory under a cooperative agreement with the NSF. THH thanks NAIC for partial sabbatical leave support during this work.

## REFERENCES

- Allen, C. W. 1973, London: University of London, Athlone Press, —c1973, 3rd ed.,
- Argyle, E. & Gower, J. F. R. 1972, BAAS, 4, 216
- Argyle, E., Baird, G., Grindlay, J., Helmken, H., & Omongain, E. 1974, Nuovo Cimento B Serie, 24, 153
- Argyle, E. 1973, ApJ, 183,
- Backer, D. C., Wong, T., & Valanju, J. 2000, ApJ, 543, 740
- Backer, D., Wong, T., Valanju, J., & Lyne, A. 1998, Bulletin of the American Astronomical Society, 30, 1151
- Bhat, N. D. R., Cordes, J. M., & Chatterjee, S. 2003, ApJ, 584, 782
- Bietenholz, M. F., Kassim, N., Frail, D. A., Perley, R. A., Erickson, W. C., & Hajian, A. R. 1997, ApJ, 490, 291
- Blandford, R. D. & Scharlemann, E. T. 1976, MNRAS, 174, 59
- Caraveo, P. A. & Mignani, R. P. 1999, A&A, 344, 367
- Cognard, I., Shrauner, J. A., Taylor, J. H., & Thorsett, S. E. 1996, ApJ, 457, L81
- Cordes, J. M. 1976, ApJ, 210, 780
- Cordes, J. M. & Hankins, T. H. 1979, ApJ, 233, 981
- Cordes, J. M. & Lazio, T. J. W. 2001, ApJ, 549, 997.
- Cordes, J. M. & Lazio, T. J. W. 2002, astro-ph/207156.
- Cordes, J. M. & McLaughlin, M. A. 2003, astro-ph/0304364.
- Cordes, J. M. & Rickett, B. J. 1998, ApJ, 507, 846
- Fesen, R. A., Martin, C. L., & Shull, J. M. 1992, ApJ, 399, 599.
- Fesen, R. A., & Kirshner, R. P. 1982, ApJ, 258, 1.
- Friedman, F. J. & Borkiakoff, V. 1985, BAAS, 17, 751
- Hankins, T. H. & Moffett, D. A. 1998, Bulletin of the American Astronomical Society, 30, 903
- Hankins, T. H., Kern, J. S., Weatherall, J. C. & Eilek, J. A., 2003, Nature, 422, 141.
- Isaacman, R. & Rankin, J. M. 1977, ApJ, 214, 214.
- Johnston, S. van Straten, W., Kramer, M. & Bailes, M. 2002, astro-ph/0101146.
- Johnston, S. & Romani, R. W. 2002, MNRAS, submitted, astro-ph/0201378.
- Kinkhabwala, A. & Thorsett, S. E. 2000, ApJ, 535, 365.
- Löhmer, O., Kramer, M., Mitra, D., Lorimer, D. R., & Lyne, A. G. 2001, ApJ, 562, L157.
- Lundgren, S. C., Cordes, J. M., Ulmer, M., Matz, S., Lomatch, S., Foster, R.S., Hankins, T., 1995, ApJ, 453, 433.
- Lyne, A. G., Pritchard, R. S., & Graham-Smith, F. 2001, MNRAS, 321, 67
- Lyne, A. G., & Thorne, D. J. 1975, MNRAS, 172, 97.
- MacAlpine, G. M. et al. 1994, ApJ, 432, L131
- McLaughlin, M. A. & Cordes, J. M. 2003, astro-ph/0304365.
- Moffett, D. A. 1997, Ph.D Thesis, New Mexico Tech.
- Moffett, D. A. & Hankins, T. H. 1996, ApJ, 468, 779
- McLaughlin, M. et al. 1999, ApJ, 512, 929.
- McLaughlin, M. et al. 2001, ApJLetts, 547, 41.
- Narayan, R. 1992, Phil. Trans. R. Soc. Lond. A 341, 151.
- Rickett, B. J. 1975, ApJ, 197, 185
- Rickett, B. J. 1990, ARA&A, 28, 561
- Romani, R. W., & Johnston, S. 2001, ApJ 557, L93
- Sallmen, S., Backer, D. C., Hankins, T. H., Moffett, D., & Lundgren, S. 1999, ApJ, 517, 460
- Schaller, E. L. & Fesen, R. A. 2002, AJ, 123, 941
- Staelin, D. H. & Reifenstein, E. C. 1968, Science, 162, 148.
- Thorsett, S. E., & Stinebring, D. 1990, ApJ 361, 644
- Trimble, V. 1968, AJ, 73, 535.

TABLE 1  
OBSERVATIONAL PARAMETERS

$\nu$ (GHz)	MJD	$T^a$ (hr)	$B$ (MHz)	$\Delta t$ ( $\mu s$ )	$\Delta\nu$ (MHz)	$\Delta t_{DM}$ ( $\mu s$ )	$S_{sys}^b$ (Jy)
0.430	52304	1.0	12.5	128	0.024	145	1262
1.180	52277	1.2	100	100	0.781	224	309
1.475	52277	1.2	100	100	0.781	115	291
2.150	52304-52306	1.3	100	32	1.562	74	79
2.330	52315	1.0	100	32	1.562	58	78
2.850	52306	1.0	100	32	1.562	32	74
3.500	52398-52412	3.5	100	64	1.562	64	41
4.150	52295-52337	2.9	100	32	3.125	21	20
5.500	52336-52411	2.3	100	32	3.125	9	20
8.600-8.800	52398-52414	3.1	100	16	3.125	2	22

<sup>a</sup> $T$  is the total time of analyzed data, whether the pulsar was detected or not.

<sup>b</sup> $S_{sys}$  includes the contribution from the Crab Nebula that takes into account flux dilution by the telescope beam.

TABLE 2  
GIANT PULSE AMPLITUDE AND TIMING STATISTICS

$\nu$ (GHz)	$T^a$ (hr)	$\bar{\phi}_{\text{ip}} - \bar{\phi}_{\text{mp}}$ (cycles)	$N_{\text{ip}}/N_{\text{mp}}$	$\dot{N}_{\text{GP}}^b$ ( $s^{-1}$ )
0.430	1.0	$0.4032 \pm 10^{-4}$	0.56	3.3
1.180	0.47	$0.402 \pm 0.001$	0.05	0.51
1.475	0.58	$0.402 \pm 0.001$	0.05	0.31
2.150	0.15	$0.403 \pm 0.002$	0.07	0.25
2.330	0.15	$0.403 \pm 0.002$	0.08	0.17
2.850	0.26	$0.404 \pm 0.003$	0.05	0.11
3.500	1.27	$0.402 \pm 0.002$	0.04	0.12
4.150	1.49	$0.394 \pm 0.002$	0.10	0.31
5.500 <sup>c</sup>	0.30	—	—	0.02
8.800	1.42	$0.380 \pm 0.001$	27	0.44

<sup>a</sup> $T$  represents the total time included in the average profiles of Figure 1, which represents only the high-S/N and RFI-free subset of the overall data.

<sup>b</sup>For frequencies  $\gtrsim 3$  GHz, the number of detected giant pulses varies significantly because of diffractive interstellar scintillation. Refractive scintillation will also alter the detection rate at all frequencies.

<sup>c</sup>At 5 GHz, there are too few interpulses detected to allow meaningful estimates of the MP to IP phase offset and number ratio.

TABLE 3  
SCINTILLATION PARAMETERS

$\nu$ (GHz)	$\Delta\nu_d$ (MHz)	$\Delta t_d$ (s)	$N_{\text{GP}}$
0.43	$< 0.024$	...	100
1.48	$< 0.8$	$25 \pm 5$	180
2.33	$2.3 \pm 0.4$	$35 \pm 5$	170
2.85	$7 \pm 2$	...	60
3.50	$15 \pm 10$	...	15

## APPENDIX

## A. FREQUENCY STRUCTURE FROM SCINTILLATING AMPLITUDE-MODULATED, POLARIZED SHOT NOISE

Frequency structure in the radio spectrum of a single pulse is caused by both the statistical properties of the pulsed radiation at the time of emission and by the interference effects of multipath propagation. A model that suffices to describe many aspects of pulsar radiation is the amplitude modulated noise model (Rickett 1975) augmented to include polarized shot-noise statistics (Cordes 1976): the amplitude-modulated, polarized shot-noise (AMPSN) model. Frequency structure of single pulses was discussed by Cordes & Hankins (1979) in terms of the AMPSN model for B0950+08. Here we amplify on their treatment to show the interplay of intrinsic and interference effects on the frequency structure. We thus develop the scintillating amplitude-modulated-shot-noise model (SAMPSN).

Recent results (Hankins et al. 2003) imply that the Crab pulsar's giant pulses are indeed comprised of individual shot nano-pulses, in conformance with the AMPSN model. Let  $\epsilon_e(t)$  be the complex, narrowband electric field emitted at the pulsar and selected by the receiving system and mixed to baseband (see, e.g., Rickett 1975; Cordes 1976). We consider, for now, just a single polarization channel. For an individual giant pulse, we describe  $\epsilon_e$  as an ensemble of  $N_s$  shot pulses having individual amplitudes,  $a_j$ , but (for simplicity) identical shapes,  $\Delta(t)$ :

$$\epsilon_e(t) = \sum_{j=1}^{N_s} a_j \Delta(t - t_j). \quad (\text{A1})$$

The width of  $\Delta(t)$  is the reciprocal of the receiver bandwidth used to form  $\epsilon(t)$ . The corresponding shot pulse at the original radio frequency has width  $\sim \nu_{\text{RF}}^{-1} \sim 0.1$  to 2 ns for our data. Each shot pulse reaches the observer along  $N_p$  paths owing to multipath propagation between the pulsar and Earth. Each path has an associated time delay,  $\delta t_p$ , and amplitude  $g_k$ . The set of paths changes on a time scale that we assume is much longer than a single spin period. Also, all propagation quantities ( $N_p$ ,  $\delta t_p$ , and  $g_k$ ) are strong functions of frequency because the refractive index is that for a cold plasma. Using the total propagation time,  $D/c + \delta t_p$ , the received electric field is

$$\epsilon(t) \propto \sum_{j=1}^{N_s} a_j \sum_{k=1}^{N_p} g_k \Delta(t - t_j - D/c - \delta t_{pk}). \quad (\text{A2})$$

Here we have ignored delays from dispersive propagation through the ISM because they are deterministic and correctable. Denoting a Fourier transform with a tilde and using the shift theorem, we find that the instantaneous spectrum is

$$I(\nu) \equiv |\tilde{\epsilon}(\nu)|^2 \propto |\tilde{\Delta}(\nu)|^2 A(\nu) G(\nu), \quad (\text{A3})$$

where  $\nu$  is the baseband frequency and

$$A(\nu) = \left| \sum_{j=1}^{N_s} a_j e^{-2\pi i \nu t_j} \right|^2 \quad (\text{A4})$$

TABLE 4  
MAXIMUM DISTANCE FOR IMPORTANCE OF NEBULAR NOISE

Telescope	$\nu$ (GHz)	G (K Jy <sup>-1</sup> )	T <sub>sys0</sub> (K)	$\epsilon^{-1/2} D_{\text{Neb}}$ (kpc)
Arecibo	0.43	15	60	30
Arecibo	1.4	11	40	30
GBT	1.4	3	30	20
VLA	0.33	2	165	< 5 <sup>a</sup>
VLA	1.4	2.8	35	< 2.3 <sup>a</sup>
ATA	1.4	2.5	50	13
LOFAR	0.2	34 <sup>b</sup>	476	20
SKA	1.4	200 <sup>c</sup>	50	120

<sup>a</sup>The VLA numbers are for the D configuration which yields the largest contribution to the system temperature from the Crab Nebula.

<sup>b</sup>The gain for LOFAR is that for an inner core of antennas that represents 75% of the total collecting area.



$$G(\nu) = \left| \sum_{k=1}^{N_p} g_j e^{-2\pi i \nu \delta t_{pk}} \right|^2. \quad (\text{A5})$$

In the limit of large  $N_s$  and  $N_p$ , we expect Gaussian statistics for the sums in the equations for  $A$  and  $G$ . Consequently,  $A$  and  $G$  will both have exponential statistics, for which  $\langle A^2 \rangle / \langle A \rangle^2 = \langle G^2 \rangle / \langle G \rangle^2 = 2$ . As is well known in the scintillation literature (e.g. Rickett 1990), scintillation fluctuations in the strong-scattering regime have exponential statistics for a point source if there is no bandwidth smoothing. Note that our formulation of amplitude-modulated noise differs from that of Rickett (1975) and Cordes (1976), who model the emitted signal as  $\epsilon_\epsilon(t) = a(t)m(t)$ , where  $a(t)$  is an envelope function that modulates the noise process  $m(t)$ . Instead, the envelope function is absorbed into the particular distribution of emission times,  $t_j$ .

To isolate the frequency structure of  $A(\nu)$  from  $G(\nu)$ , one must take into account their characteristic time scales. It is reasonable to assume that the pattern of shot pulses in  $\epsilon(t)$  does not repeat. On a physical basis, such shot pulses may result from the sweeping of relativistic beams through the LOS or they may represent *bona fide* temporal modulations. Either way, on time scales  $\gtrsim P/2\pi$  ( $P$  is the pulsar period), we expect the relativistic plasma flow in the pulsar magnetosphere to have reorganized completely. The scintillation pattern, on the other hand, is sustained. It is usually true for pulsars that if the scintillation frequency structure is resolved by the spectrometer, it persists over time scales of seconds to hours, depending on the pulsar and frequency. For heavily scattered pulsars, the frequency structure is too fine to resolve and the scintillation time is accordingly short. Thus, for most pulsars, the frequency structure in  $G(\nu)$ , if resolved, is characterized by averaging  $I(\nu)$  over many individual pulses and then performing a correlation analysis to determine the characteristic bandwidth.

For the Crab pulsar, which emits giant pulses only sporadically, it is more difficult to separate  $A(\nu)$  from  $G(\nu)$  and also estimate the scintillation time scale. For an individual giant pulse,  $A(\nu)$  and  $G(\nu)$  both contribute to the observed frequency structure and with similar statistics. However, the characteristic width of  $G(\nu)$  scales strongly with frequency, as discussed above, while  $A(\nu)$  is associated with the temporal widths of the giant pulses and may be less frequency dependent.

#### Statistics for a Single Polarization Channel

Some useful statistics of the SAMPSN model are as follows. The modulation index of the spectrum  $I(\nu)$  is  $\sigma_I / \langle I \rangle = 3$  when  $A$  and  $G$  both have exponential statistics. For a pair of pulses for which  $A(\nu)$  has decorrelated completely while  $G(\nu)$  is perfectly correlated, we expect the cross correlation to be  $\rho_{12} = \langle \delta I_1(\nu) \delta I_2(\nu) \rangle / \sigma_I^2 = 1/3$ . The correlation coefficient will decline to zero on a time lag between the pair of pulses determined by the characteristic scintillation time, defined as the lag at which the correlation coefficient is  $e^{-1}$  of its maximum value of  $1/3$ .

The autocorrelation function (ACF) of the spectra for single pulses can be written in the form

$$R(\delta\nu) = \langle I(\nu)I(\nu + \delta\nu) \rangle = R_{|\bar{\Delta}|^2}(\delta\nu)R_A(\delta\nu)R_G(\delta\nu). \quad (\text{A6})$$

$R_{|\bar{\Delta}|^2}(\delta\nu)$  is a broad function that is the ACF of the bandpass filter used to form  $\epsilon(t)$ , while  $R_A$  and  $R_G$  can be much narrower and are of the form  $R_X(\delta\nu) = \langle X \rangle^2 [1 + m_X^2 \rho_X(\delta\nu)]$ , where  $m_X = 1$  for exponential statistics and  $\rho_X(0) = 1$ . The intensity correlation function,

$$R(\delta\nu) = \langle G \rangle^2 \langle A \rangle^2 R_{|\bar{\Delta}|^2}(\delta\nu) [1 + m_A^2 \rho_A(\delta\nu)] [1 + m_G^2 \rho_G(\delta\nu)], \quad (\text{A7})$$

will typically have a narrower component and a broader component associated with  $\rho_A$  and  $\rho_G$ , respectively, or vice versa. The total squared-modulation index is  $m^2 = \sigma_I^2 / \langle I \rangle^2 = R(0) / \langle G \rangle^2 \langle A \rangle^2 R_{|\bar{\Delta}|^2}(0) - 1 = 1 + m_A^2 + m_G^2 = 3$ . If the data are channelized with channel bandwidths larger than the characteristic bandwidth of  $A$  or  $G$ , the modulation index will be reduced.

Some giant pulses comprise a small number of shot pulses,  $N_s \approx$  a few, in which case  $A(\nu)$  will have non-exponential statistics. For example, for two equal-amplitude shot pulses separated by  $\Delta t_{12}$ ,  $A(\nu) \propto (1 - \cos 2\pi\nu\Delta t_{12})$ . If  $\nu\Delta t_{12} \gg 1$ , we would have  $m_A = 2^{-1/2}$  and the spectral shape would be oscillatory. In the limit of a single shot pulse (or a cluster of shot pulses contained within an interval smaller than the reciprocal bandwidth), the modulation across the bandwidth would derive solely from  $G$ , the scintillation factor.

#### Statistics for the Total Intensity

When two polarization channels are summed to yield the total intensity, as in the analysis of this paper, the statistics are altered. Scintillations are identical for the two polarizations while the frequency structure from the AMPSN will differ according to the degree of polarization. If the signal is 100% polarized, the total intensity will have the same statistics as that of a single polarization channel containing the signal, while for an unpolarized signal, the AMPSN spectral fluctuations will be reduced by  $\sqrt{2}$ .

Letting  $d_p$  equal the total degree of polarization (linear and circular), it may be shown (Cordes 1976) that the intensity modulation index is now (in the limit of Gaussian statistics for a single polarization channel)

$$m_I^2 = m_G^2 + (1 + m_G^2)(1 + d_p^2)/2 \stackrel{m_G=1}{=} 2 + d_p^2, \quad (\text{A8})$$

where the last equality holds for  $m_G = 1$ . Now, when the total intensity spectra of pulse pairs are cross-correlated, we have

$$\rho_{12} = \langle \delta I_1(\nu) \delta I_2(\nu) \rangle / \sigma_I^2 = \frac{m_G^2}{m_G^2 + (1 + m_G^2)(1 + d_p^2)/2} \stackrel{m_G=1}{=} \frac{1}{2 + d_p^2}. \quad (\text{A9})$$